Received: 23 December 2019 | Revised: 13 April 2020 | Accepted: 5 May 2020

DOI: 10.1002/ese3.741

RESEARCH ARTICLE

Energy Science & Engineering
Open Access

A tool to minimize the need of Monte Carlo ray tracing code for 3D finite volume modelling of a standard parabolic trough collector receiver under a realistic solar flux profile

Majedul Islam[1] | **Suvash C. Saha**[2] | **Prasad K. D. V. Yarlagadda**[1] | **Azharul Karim**[1]

[1]School of Mechanical Medical and Process Engineering, Queensland University of Technology, Brisbane, QLD, Australia

[2]School of Mechanical and Mechatronic Engineering, University of Technology Sydney, Australia

Correspondence
*Majedul Islam and Azharul Karim, School of Mechanical Medical and Process Engineering, Queensland University of Technology, Brisbane, QLD 4001, Australia.
Emails: i.majedul@qut.edu.au; murad99me@yahoo.com(MI); azharul.karim@qut.edu.au(AK)

Abstract

The energy collection element of a parabolic trough collector includes a selective coated metallic receiver tube inside an evacuated glass tube. Perpendicularly incident sun light on the parabolic trough mirror aperture is concentrated on the receiver tube highly nonuniformly along its circular direction. This solar energy is collected as thermal energy circulating a suitable heat transfer fluid (HTF) through the tube. This conjugate heat transfer phenomenon under nonuniform heat flux boundary condition is computationally studied applying 3D finite volume (FV) modelling technique of computational fluid dynamics coupled with Monte Carlo ray tracing (MCRT) optical data. The MCRT model simulates the actual flux profile around the receiver tube. Apart from a FV model, this coupled study requires expertise in, and access to, a suitable MCRT code. A combination of polynomial correlations and user-defined function (UDF) is introduced in this article in order to minimize the need of MCRT codes from subsequent FV modelling of the receiver tube of the Luz Solar 2 (LS2) collector. The correlations are developed from a verified 3D MCRT model, which is equivalent to the local irradiation data as a function of receiver circular location. The UDF includes two algorithms: one to develop solar flux profile from the correlations around the receiver, and the other to calculate heat loss from the receiver. Interpreting the UDF into ANSYS Fluent, a 3D FV model of the LS2 receiver is developed and validated with experimental results. The effectiveness of the UDF as an alternative to MCRT code is verified. The FV model is capable to investigate the heat transfer characteristics of the LS2 collector receiver at different solar irradiation level, optical properties of the collector components, glass tube conditions, HTFs, inserts or swirl generators, collector length, and internal diameter of the tube.

KEYWORDS

computational fluid dynamics, concentrating solar power, finite volume, Luz Solar 2 collector, Monte Carlo ray tracing, parabolic trough collector

1 | INTRODUCTION

Rapid depletion of fossil fuel, global warming, and ecological imbalance act as driving factors to use green and renewable alternatives of energy like solar. Efficient harnessing of this literally in-exhaustive energy has the capacity to fulfill world's energy demand.[1,2] Significant amount of research already been undertaken to develop technologies for harnessing this abundant energy.[3-22] Concentrating solar power (CSP) technologies including the parabolic trough collector (PTC), parabolic dish, linear Fresnel reflector, and heliostat field are competitive candidates to the conventional sources in terms of carbon emissions though the investment cost is still higher.[23]

The PTC is one of the most efficient CSP technologies for medium temperature application ranging between 50°C and 400°C.[1,24-26] A PTC consists of a parabolic trough mirror and an energy collection element (ECE) placed along the focal line of the mirror as shown in Figure 1. The PTC can be either east-west oriented, tracking the sun from north to south collecting maximum energy in winter, or north-south oriented, tracking the sun from east to west collecting maximum energy in summer employing a single-axis tracking system.[1,26,27] Perpendicularly incident light rays on the aperture of a solar pointed collector are reflected from the trough and concentrated on to the ECE. The concentrated radiation heats up the continuously circulated heat transfer fluid (HTF) through the receiver tube (see Figure 1), and, by this way, incident solar energy is converted into useful thermal energy. Thus, the overall energy performance of the collector directly depends on the optical performance of the collector and heat transfer performance of the ECE.[25,28,29]

The optical performance of the collector involves parameters including solar concentrated irradiance distribution on the outer surface of the receiver tube, average light concentration, optical efficiency, and light intercept factor. Different optical and physical factors like solar irradiance intensity, ECE geometry, optical properties of the collector components, "dirt and dust" on the components, receiver defocus, and tracking error[29-31] affect the optical and thermal performance of the collector. The irradiance distribution around the receiver tube is highly nonuniform, which can be determined experimentally applying flux mapping[32,33] and theoretically applying cone optics,[30,34,35] and, most popularly, applying Monte Carlo ray tracing (MCRT) technique.[29,36-43]

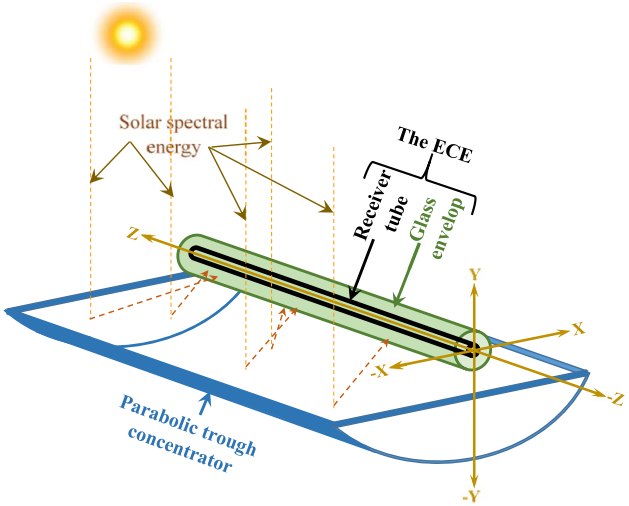

FIGURE 1 A typical parabolic trough solar collector

On the other hand, thermal performance of the collector depends on the ECE design, optical and thermal properties of the receiver material, flow characteristics of the HTF, heat removal factor, heat loss coefficient, and operating and ambient condition of the collector.[1,26,27,31,37,44-53] The receiver tube is usually coated with selective coating in order to absorb most of the concentrated light. A glass tube envelop around the receiver tube is usually placed to reduce convection loss. The loss can be further reduced evacuating the annular space between the glass tube and the receiver tube. Most of the spectral energy of the radiation is absorbed in the selective coating that increases the temperature and heat flux density at the outer surface of the receiver tube. Due to the temperature gradient, thermal conduction occurs in the tube material, and heat fluxes become available at the inner surface of the tube. The heat flux from the inner surface is absorbed into the HTF, transferred by means of mass transfer of the fluid, and released into a heat exchanger for storage or desired application. Heat conduction at the solid-fluid interface and heat convection in the bulk fluid take place. The energy transfer from the tube surface to the HTF is a coupled heat and mass transfer phenomenon with complex geometry condition.[26]

With technological advancement in computing tools, modelling and simulation of PTC system provide useful information on the collector performance and optimization with less uncertainty, effort, and cost than their experimental counterpart.[3] The collector systems were studied numerically by many researchers.[3,12]

Applying 1D approach, Forristall [31] investigated the effect of design conditions and operating parameters on the thermal performance of the ECE of a PTC. Luz black chrome, cermet, and solel cermet selective coatings were studied, and the ECE showed improved thermal performance. Gercia and Velazquez[54] developed a 1D mathematical model considering the geometrical, optical, thermal, and fluid dynamic aspects of a single-pass and double-pass of the HTF through the ECE. They obtained improvement in heat transfer operating the solar PTC with external recycle or with a double-pass without recycle. Padilla et al[55] developed a detailed 1D numerical model of an ECE to calculate heat losses and collector efficiency under different flow, selective coating, and operating conditions. Kalogirou[27] presented a detailed mathematical model of an ECE written in Engineering Equation Solver (EES) and validated against known performance of

existing collectors tested in Sandia National Laboratories (SNL). Similarly, Yilmaz and Soylemez[56] also presented a discretized thermo-mathematical modelling of the ECE to calculate heat losses and collector efficiency under different flow, selective coating, and operating conditions. Behar et al[25] presented a novel 1D thermal resistance-based model and compared against test results conducted by the SNL and National Renewable Energy Laboratories (NREL). Liang et al[57] summarized the 1D mathematical models under different assumptions and proposed a simple algorithm to make the control equations linear and solve easily. All of these 1D models are suitable for a single-piece short ECE under the assumptions that the solar radiation flux, wall temperature, and physical properties are uniform for the whole ECE circumference. However, 1D model is unable to capture nonlinearity in temperature along the ECE axis and, therefore, may underestimate heat losses.[31]

Forristall[31] implemented a 2D mathematical model of the ECE of Luz Solar 2 (LS2) collector in engineering equation solver (EES) to investigate its heat transfer characteristics. The model was verified with test result obtained by Dudley et al.[47] Tao and He[58] presented a unified 2D numerical model for the coupled heat transfer process in PTC receiver tube. Both of these studies assumed constant heat flux on the outer surface of the receiver tube. On the contrary, Hachicha et al[59] developed a 2D finite volume (FV) model of the ECE coupled with optical model enabling nonuniform solar flux distribution around the ECE. The 2D model of Wang et al[60] also capable to account asymmetric characteristics including nonuniform heat flux, eccentric configuration, and incident angle. Coupling a 3D optical model, Huang et al[61] proposed a 2D model in order to calculate heat loss more quickly and accurately. While a 2D model is sufficient to investigate the conjugate heat and mass transfer phenomenon of the ECE, a 3D model, on the other hand, allows visualization and provides in-depth insight of the physics. Up until now, only a handful of studies have focused on 3D thermo-fluid characteristics of HTF inside the tube of a PTC considering evacuated glass envelop and realistic nonuniform heat flux boundary conditions.

Ya-Ling He et al[38] coupled a MCRT model with a finite volume (FV) model for CFD study, and studied the 3D HTF flow field and temperature distribution in the receiver tube of the ECE. Similarly, Wirz et al[62] and Tao and He[36] also coupled a FV solver with MCRT model to study solar flux nonuniformity effect on the radiative exchange between the participating surfaces, and heat loss and gain.

The overall goal of these early studies was to explore the conjugate heat transfer characteristics of the ECE under realistic solar flux profile relying on coupled MCRT and CFD model. This coupled study is computationally expensive, and relied on access to, and expertise in MCRT codes, and prohibitive to many CFD researchers. No study could be found in the literature that attempted to either eliminate or minimize the need of this MCRT code for the study. The authors attempted to address this research gap and made endeavor to provide a tool to minimize the need of an MCRT code.

The MCRT simulates the optical interactions among the participating surfaces, which is a surface phenomenon and temperature independent, whereas the FV model accounts for volumetric effect of the heat flux and temperature dependent. Depending on the glass envelop condition, the annuli space between the receiver tube and the glass tube is either evacuated, filled with air, or open to environment. As the solar heat flux boundary condition is the direct input to the FV model from the MCRT model, for each variation in optical conditions including daily normal irradiance, glass tube conditions, and optical properties of the collector materials, the MCRT needs to be executed in parallel to the FV model. By this way, the process becomes computationally highly expensive.

Therefore, studying the optical characteristics of a standard PTC using MCRT technique, the authors have developed optical design data in the form of polynomial correlations and MCRT-FV coupling algorithm. The correlations and the coupling algorithm altogether replace the MCRT for further CFD study using FV model of the receiver of the collector.

The correlations for nonuniform solar flux were developed in terms of local concentration ratio (LCR) from a verified MCRT model developed earlier by the authors.[29] LCR is a nondimensional value, which is a function of receiver angular location, and product of daily normal irradiation, optical properties of the collector components and other factors that have linear effect on the optical properties of the collector. A user-defined function (UDF) was then written using Fluent-specific programming language incorporating the correlations and heat loss functions, and was interpreted in the ANSYS Fluent.

It is assumed that the solar incidence is perpendicular to the collector aperture, and the receiver diameter and the trough width are fixed to those of the modelled standard collector. Based on these assumptions, the UDF is capable to produce realistic nonuniform solar flux profile around the wall boundary of the receiver and calculate heat loss from the outer surface of receiver adopting the following variations in:

1. optical conditions include daily normal irradiance, optical properties of the collector components and linear optical loss factors such as tracking error, and effect of dirt and dust on the participating surfaces;
2. collector geometry that include collector length and internal diameter of the receiver;
3. glass envelop conditions including evacuated, filled of air or removed; and
4. internal design of the receiver, HTFs, and ambient conditions.

In order to be able to validate the MCRT and FV models directly, the LS2 parabolic trough collector from Dudley et al[47] was modelled. Zemax optical ray-tracing software for MCRT modelling[29] and ANSYS Fluent 15.0[63] for FV modelling were employed.

2 | PHYSICAL MODEL

The LS2 collector was used in the Solar Energy Generating System III-VII 150 MW plants, Kramer Junction, California, USA. It was tested on the AZTRAK rotating platform at SNL.[47] Figure 2A,B show the cross-sectional views of the collector and the ECE. The geometry and the optical properties of the collector are given in Table 1. A closed-end plug was inserted in the tube of the collector to increase the flow velocity of the HTF, Sylltherm800 silicone oil. Thermal performances of the collector for evacuated, lost evacuated, and removed glass envelop conditions were measured using black chrome or cermet selective coatings for varying weather conditions. For the MCRT modelling, the trough and the ECE with and without glass tube envelop excluding the support structure of the LS2 collector were modelled, whereas only the HTF domain was modelled for the current FV simulation as discussed in the following sections.

3 | IRRADIANCE DISTRIBUTION AROUND THE ECE

3.1 | MCRT modelling

The detail MCRT simulation technique is available in,[29] and a brief description is given in this section as follows.

The Cartesian coordinate system, *XYZ*, was used for the trough and the cylindrical coordinate system, and *rβZ* was adopted for the ECE system. The LS2 collector was modelled as per the geometry as presented in Table 1. A biconic surface for the parabolic trough and two concentric annular volume objects for the receiver tube and the glass tube from the object library of the software package were adapted to model the collector system. The ECE was 100 mm larger than the trough at both ends. Ideal coating system was enabled, and desired specular reflectance of the mirror, glass transmittance with antireflection coating, and ECE absorptance with spectral selective coatings were developed. The ray tracing algorithm and the light interaction among the components are presented in Figure 3A,B, respectively.

The steps in Figure 3A are self-explanatory. The rhombuses and rectangles in the flow chart represent the arguments and Monte Carlo decision of the arguments, respectively. The Monte Carlo decision was based on the sunshape, optical properties and geometry of the collector components, and the laws of reflection and refraction. The azimuth angle and the deflection angle of the sunshape, $I(\varphi)$, see Equation (1), were 2π and 0.266°, respectively. The incident location and the direction vectors of the rays were denoted by $P(P_x, P_y, P_z)$ and $D(D_x, D_y, D_z)$, respectively. Considering the computational expense and an average absolute error of 0.1 to 0.08% in the concentrator reflectance and the glass transmittance, 5×10^7 to 10×10^7 rays/m^2 of aperture area of the collector were traced for the model. Light reflection on the mirror and transmission through the glass was followed by Fresnel's law, Equation (2), and Snell's law, Equation (3).

$$I(\varphi) = \frac{\cos\left(\frac{0.05868\varphi}{\pi}\right)}{\cos\left(\frac{0.05868\varphi}{\pi}\right)} \tag{1}$$

where φ is the deflection angle.

$$D_{PT} = D_n - 2\left(N_{PT} \cdot D_n\right) N_{PT} \tag{2}$$

$$D_{GT} = D_{PT} - \left(N_{GT} \cdot D_{PT}\right) N_{GT} + \sqrt{(n_{GT})^2 - (n_{air})^2 + \left(N_{GT} \cdot D_{PT}\right)^2} N_{GT} \tag{3}$$

where D, N, n_{GT}, and n_{air} are the direction vector, normal vector, and refractive indices of the glass and air, respectively. The normal vectors, N_{PT} and N_{GT}, were calculated from Equations (4) and (5), respectively.

$$N_{PT} = \frac{-P_{y\_PT}}{\sqrt{P_{y\_PT}^2 + 4f^2}} j + \frac{2f}{\sqrt{P_{y\_PT}^2 + 4f^2}} k \tag{4}$$

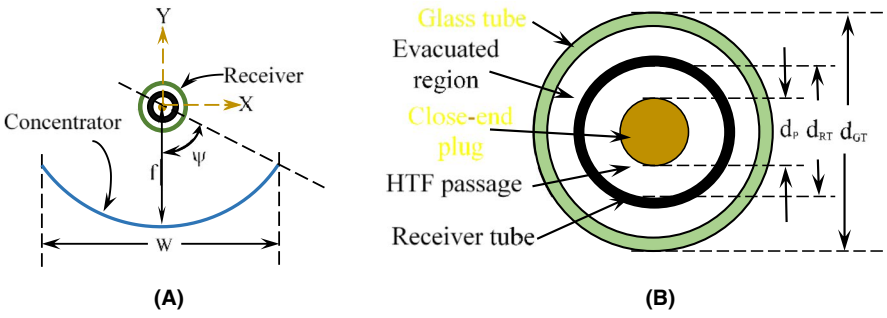

FIGURE 2 Cross-sectional views of (A) the Luz Solar 2 (LS2) collector and (B) the ECE geometry

TABLE 1 Geometric configuration, optical properties and loss factors of the Luz Solar 2 parabolic trough collector[31]

Parameters	Value
Concentrator width, W=	5 m
Concentrator length, L_{PT}=	7.8 m
ECE length, L_{RT}=	8 m
Rim angle, ψ=	≈70°
Focal length, f=	1.84 m
Close-end plug outer diameter, d_P=	50.8 mm
Glass tube outside diameter, d_{GT}=	115 mm
Glass tube thickness, t_{GT}=	3 mm
Receiver tube inside diameter, d_{RT}=	66 mm
Receiver tube thickness, t_{RT}=	2 mm
Outside diameter of the HTF annulus, $(D_{HTF})_{max}$=	50.8 mm
Inside diameter of the HTF annulus, $(D_{HTF})_{min}$=	50.8 mm
Concentrator reflectance, ρ_{PT}=	0.9337
Glass tube transmittance, $\tau_{GT,}$ for evacuated condition= and for bare ECE=	0.935 1.0
ECE absorptance, $\alpha_{RT,}$ for (mostly used) cermet selective coating= black chrome selective coating=	0.92 0.94
Tracking error factor, E_σ=	0.994
Geometry error factor, E_{geom}=	0.98
General error factor, E_{gen}=	0.96
Optical loss factor for dirt on receiver tube=	0.981
Optical loss factor for dirt on parabolic trough=	0.963

Note: In the table, suffix PT, RT, P, GT, max, min, σ, geom and gen refer the parabolic trough, Receiver tube, close ends plug as flow restriction device, glass tube, maximum, minimum, sigma (tracking error in degree), geometry, and general, respectively.

$$N_{GT} = \frac{P_{y\_GT}}{\sqrt{P_{y\_GT}^2 + P_{z\_GT}^2}} j + \frac{P_{z\_GT}}{\sqrt{P_{y\_GT}^2 + P_{z\_GT}^2}} k \quad (5)$$

where P is the incident points of the rays in Cartesian coordinate system and f is the focal length of the mirror.

$$\mathrm{LCR} = \frac{I(\beta)}{DNI \times C_{opt}} \quad (6)$$

$$C_{opt} = C_{opt\_1} \times E_\sigma \times E_{geom} \times E_{gen} \times \text{Dirt on RT} \times \text{Dirt on PT} \quad (7)$$

$$C_{opt\_1} = \rho_{PT} \times \tau_{GT} \times \alpha_{RT} \quad (8)$$

3.2 | MCRT model validation

The MCRT model was validated against the measured optical efficiency of the LS2 collector[47] and analytical irradiance distribution developed by Jeter for his exemplary collector.[30,34,35] Several test conditions of the LS2 collector (see Table 2) were modelled, and optical efficiencies were calculated using the current MCRT model (shown in Figure 4A). Jeter's published analytical model is able to predict local irradiance intensity, I(β), in angular direction of the ECE as local concentration ratio (LCR) using Equation (6). The factors product, $C_{opt,}$ was assumed unity. The LCR profiles of an ideal collector of 20 × geometric concentration (GC) and 90° rim angle with a 3 mm thick glass tube envelop and without glass tube were calculated using the current MCRT model and compared against Jeter's one as shown in Figure 4B. The light intensity was one sun (1 kW/m^2), and angular radius of the solar disk was 7.5 mrad. Figure 4 shows very good agreement between the MCRT calculated results and literature.

3.3 | Correlations to calculate irradiance distribution around the bare ECE

Extensive MCRT investigation confirms that the LCR profile of the ECE of an ideal PTC is bisymmetric with respect to the geometric symmetry of the collector, that is, the global YZ plane (see Figure 4B). Refer to Figure 4B, normal LCR profile is symmetric about the geometric symmetry of the collector and assumed uniform along the length of the ECE. As presented in Figure 5, the profile can be divided as (A) ECE shadowing zone within $0° \leq \beta \leq 15°$, (B) concentration increasing zone within $15° < \beta \leq 48°$, (C) concentration falling zone within $48° < \beta \leq 90°$, and (D) direct sun zone within $90° < \beta \leq 180°$. Moreover, the LCR was found proportional to the DNI and optical properties of the collector components including the mirror reflectance, glass transmittance, and the receiver tube absorptance.[29] Ignoring the effect of glass envelop refraction on the flux profile, a set of polynomial correlations for the collector to calculate the LCR as a function of angular location, β (°), of the receiver tube was developed as given in Table 3. From the LCR, the local irradiance profile, I_β, around the ECE can be calculated using Equation (6), (7), and (8) as shown in Figure 6.

4 | FINITE VOLUME MODELLING

4.1 | The computational domain and its physical properties

Selected test conditions, in which the glass envelop was either broken or removed, are presented in Table 4. Since the LCR profile was bisymmetric with respect to the global YZ plane, characteristics of physical symmetry in the HTF domain were utilized to minimize the computational

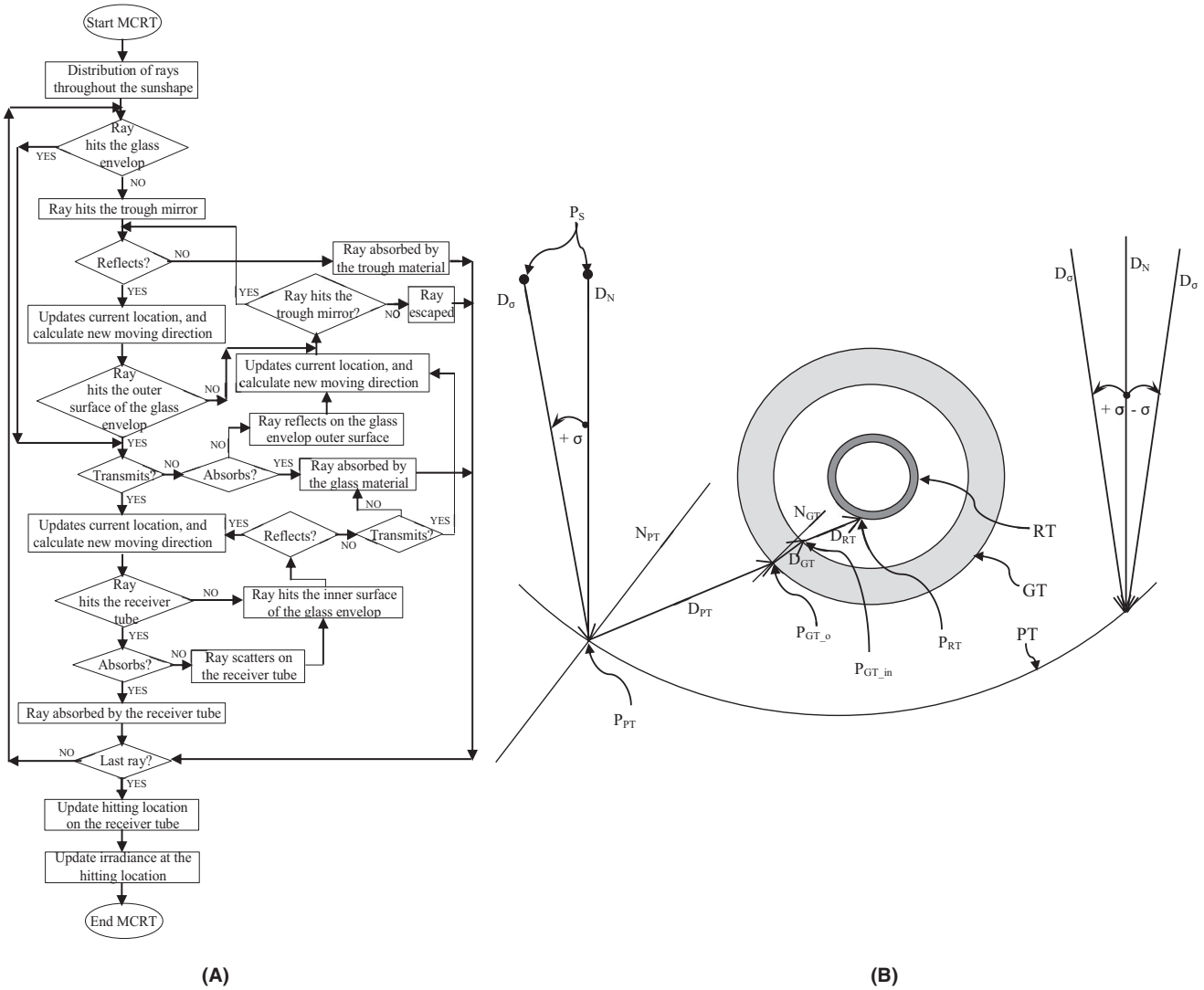

FIGURE 3 Algorithm for the Monte Carlo ray-tracing model of LS2 Collector: (A) flowchart and (B) direction vectors of the incident rays (in the figure, P, D, and N stand for light incident points, direction vectors and normal vector, respectively, whereas the suffixes, *s*, *σ*, *N*, PT, GT, RT, *o*, and in are stand for sun tracking error in degree, normal, parabolic trough, glass tube, receiver tube, outer or outside, and inner or inside, respectively)

TABLE 2 Test conditions for the MCRT model[47]

Sl No.	DNI (W/m^2)	Selective Coatings	Glass Tube Condition	η_{opt} (%)	E_{est} (%)
1	807.9	Cermet	Vacuum	72.63	1.91
2	925.1	Cermet	Air filled	73.68	1.96
3	954.5	Cermet	Removed	77.5	-
4	850.2	Black Chrome	Vacuum	73.1	2.36

Note: In the table, DNI is daily normal irradiation, η_{opt} is optical efficiency, and E_{est} is estimated experimental error.

expense with fewer grids. The computational domain between the close-end plug and the receiver tube is a semi-cylindrical horizontal annulus, see Figure 2B, as presented in Figure 7. Kelvin temperature (K)-dependent thermal conductivity of the ECE material, stainless steel, is given by Equation (9a),[64] and thermo-physical properties include density (ρ), heat capacitance (C_P) and thermal conductivity (k), and dynamic viscosity (μ) of the HTF, Syltherm800 oil, are adapted from reference,[65] and given by Equations from (9a) to (9e).

$$k_{st} = 15.906 + 2.5\times10^{-3}T + 5\times10^{-5}T^2 \quad (9a)$$

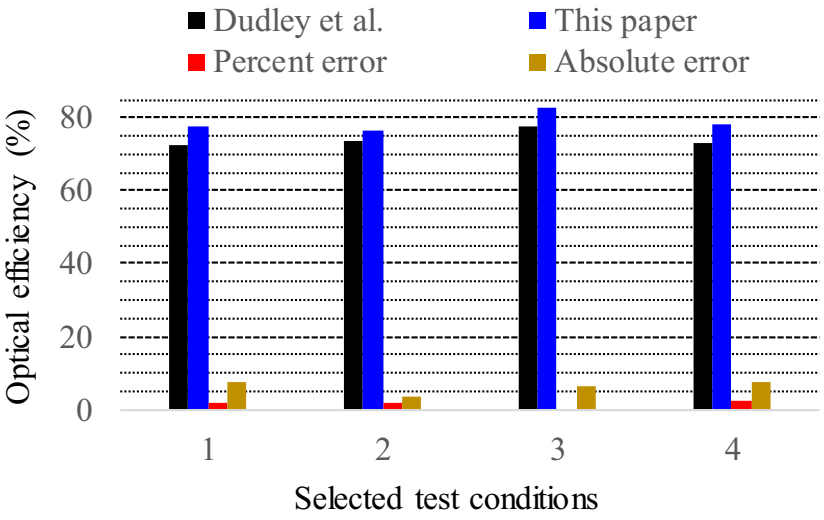

(A)

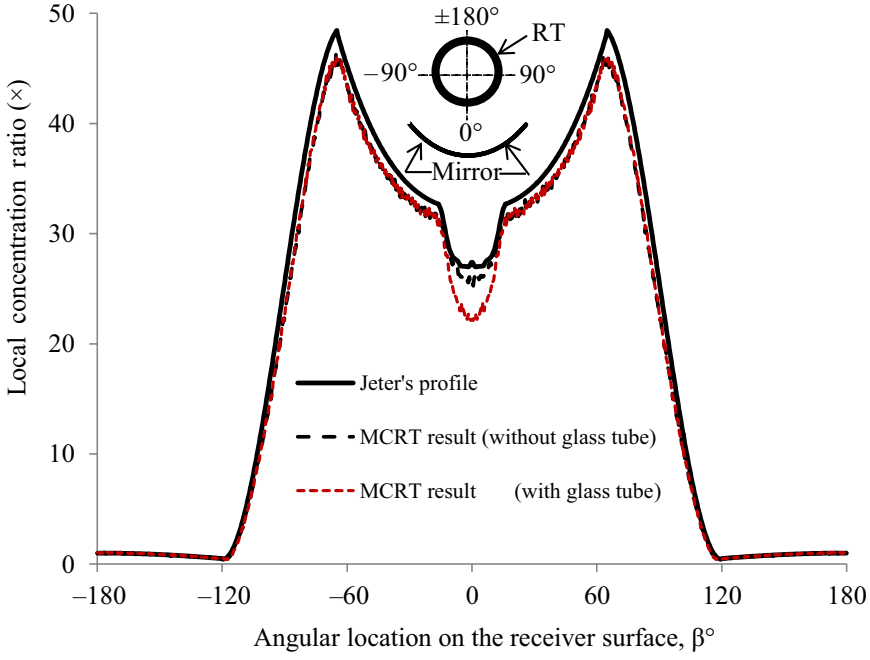

(B)

FIGURE 4 Validation of the MCRT model. A, Near-optical efficiency measured by Dudley et al vs MCRT calculated optical efficiency in this paper and B, MCRT predicted LCR profile in this paper vs Jeter's analytical profile. In the figure, RT means receiver tube

$$\rho = 1139.2 - 0.546T - 4.87\times10^{-4}T^2\ (233\text{K} \le T \le 673\text{K}) \quad (9b)$$

$$C_P = 1108.2 + 1.7073T\ (233\text{K} \le T \le 673\text{K}) \quad (9c)$$

$$\begin{aligned}\mu &= 0.157 - 8\times10^{-4}T + 1.03\times10^{-6}T^2\ (233\text{K} \le T \le 340\text{K})\\ &= 0.0848 - 5.54\times10^{-4}T + 1.39\times10^{-6}T^2 - 1.57\times10^{-9}T^2 + 6.67\times10^{-13}T^2\ (340\text{K} < T \le 673\text{K})\end{aligned} \quad (9d)$$

$$k = 0.1901 - 1.88\times10^{-4}T\ (233\text{K} \le T \le 673\text{K}) \quad (9e)$$

4.2 | Boundary conditions

The boundaries are showed in Figure 7. As the HTF was viscous, the wall surfaces formed by the ECE and the plug were considered no-slip, that is, near the wall,

$$u = v = w = 0 \quad (10)$$

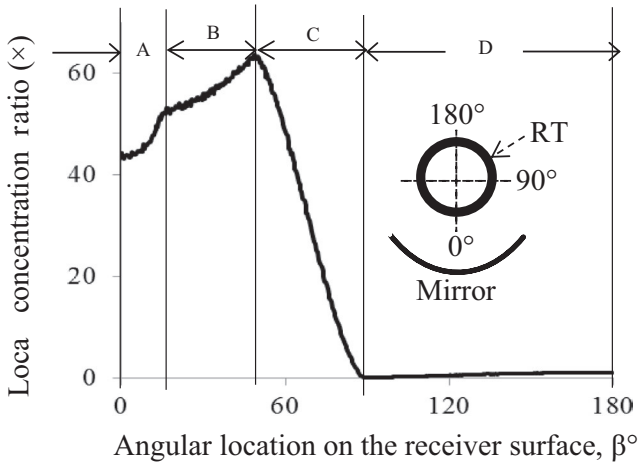

FIGURE 5 Characteristics of the LCR profile of the LS2 collector ECE at ideal condition

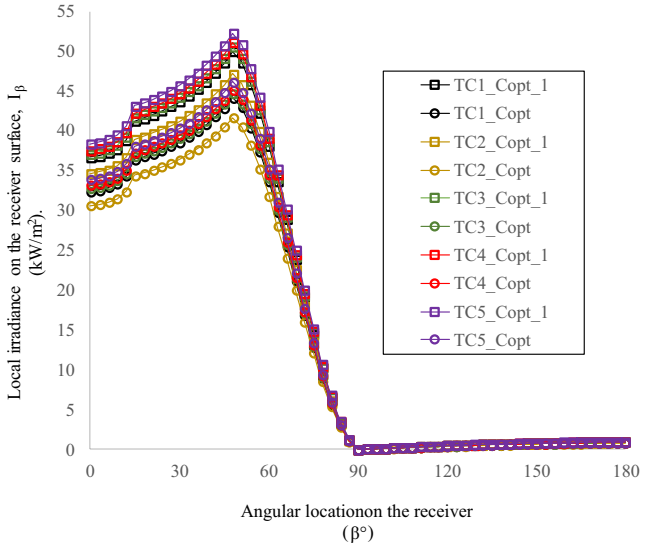

FIGURE 6 Calculation of the irradiance flux profile, $I(\beta)$, across the surface of the ECE employing the correlations given in Table 3. (In the legend of the figure, TC1, TC2, etc, refer the test conditions of Table 4. C_{opt} and C_{opt_1} are defined by Equations (7) and (8), respectively. The values of the factors are given in Table 1)

Launder and Spalding standard wall functions were used for near wall treatment.[66] The wall was not modelled. However, a thickness of 3 mm was considered for the wall, and the shell conduction was checked in the model.

At steady-state condition, the plug wall was assumed adiabatic in radial direction, that is,

$$\frac{\partial T(r\beta Z)}{\partial r}=0, \quad \text{but} \frac{\partial T(r\beta Z)}{\partial \beta}\neq 0 \neq \frac{\partial T(r\beta Z)}{\partial Z} \tag{11}$$

where $r\beta Z$ is cylindrical coordinate system.

Since, the light is concentrated on the ECE surface, at steady-state condition, this surface was assumed as constant heat flux wall, that is,

$$-k_{st}\frac{\partial T}{\partial r}\Big]_{r=R}=I(\beta) \tag{12}$$

where R is the radius of the receiver tube.

As the computational domain was essentially a part of a long pipe flow, at the inlet and outlet, the flow was considered fully developed velocity inlet and fully developed pressure outlet, respectively, that is, the flow along the tube (Z direction) at the inlet and outlet was characterized as:

$$\frac{\partial w(r\beta Z)}{\partial z}=0 \quad \text{or} \frac{\partial w(XYZ)}{\partial z}=0 \tag{13}$$

A "symmetry" boundary condition was assumed along the YZ plane, such as:

$$d(u,v,w,T,P,k,\varepsilon)=0 \tag{14}$$

The rest of the HTF flow line beyond the computational domain was assumed perfectly thermally insulated. The edges of the walls at the inlet and outlet of the domain were assumed adiabatic. Heat loss from the frame and bracket of the domain was neglected.

TABLE 3 Polynomial correlations to calculate irradiance distribution around the bare ECE of the LS2 collector

β limit[a] (°)	LCR	R^2 value
$0°\leq\beta\leq 15°$	$=0.000198\beta^4-0.003\beta^3+0.0237\beta^2+0.0359\beta+46.453$	0.9857
	$=0.0028\beta^3-0.0129\beta^2+0.1333\beta+43.333$[b]	0.9973
$15°<\beta\leq 48°$	$=0.000119\beta^3-0.0041\beta^2+0.2074\beta+49.602$	0.997
$48°<\beta\leq 90°$	$=0.00123043\beta^3-0.2511\beta^2+15.012\beta-214.19$	0.9999
$90°<\beta\leq 180°$	$=-0.0001055\beta^2+0.0419\beta-2.9121$	0.9954

[a]β is angular location on the ECE that varies from 0° to 180° for these correlations. However, the flux profile for the rest of the ECE is the mirror image of the given profile by the respective correlation.

[b]If a glass tube around the receiver tube is considered. Glass envelop causes shading effect around ±15° of the ECE. The effect of glass refractance on the profile beyond ±15° is neglected.

TABLE 4 Selected test conditions for the FV modelling (Dudley, Kolb[47])

Test conditions	DNI (W/m^2)	T_{amb} (°C)	T_{in} (°C)	v_{HTF} (m/s)	Re	T_{out} (°C)	v_{amb} (m/s)
1	919	22.6	301.4	0.608157	12 710.1	318	0.1
2	867.6	19.8	203.4	0.597403	6431.098	219.6	0.5
3	929.8	21.8	252.2	0.606962	9218.136	269	1
4	941.1	13.5	313.1	0.667897	14 950.33	322	8
5	961.3	15.1	313.3	0.667897	14 967.46	320.7	9.3

4.3 | Grid generation

The generated grids were structured and hexahedral in shape as shown in Figure 8. As the flow was turbulent and viscous, the grid size was uniform along the flow (Z direction) and inflated across the flow (radial direction). The inflation rate from wall to the center of the flow was 10%, and the $y+$ value near the wall was reasonably small to capture the physics near the walls.

4.4 | Governing equations

Considering the critical Reynolds number, Re_c, is 4000 for close channel flow through a tube or annulus, the flow of the HTF of the selected test conditions of Table 4 at steady-state condition was categorized as steady-state and incompressible turbulent flow. The governing equations for this particular flow criterion are given below.[63]

As the flow was assumed incompressible, the volume continuity equation replaced the mass continuity equation.

$$\nabla \cdot u_i = \frac{\partial u}{\partial x} + \frac{\partial v}{\partial y} + \frac{\partial w}{\partial z} = 0 \tag{15}$$

The momentum equations were as follows while the gravity was acting along the –YY axis:

$$\rho\left(u\frac{\partial u}{\partial x} + v\frac{\partial u}{\partial y} + w\frac{\partial u}{\partial z}\right) = -\frac{\partial p}{\partial x} + (\mu + \mu_t)\left(\frac{\partial^2 u}{\partial x^2} + \frac{\partial^2 u}{\partial y^2} + \frac{\partial^2 u}{\partial z^2}\right) \tag{16a}$$

$$\rho\left(u\frac{\partial v}{\partial x} + v\frac{\partial v}{\partial y} + w\frac{\partial v}{\partial z}\right) = -\frac{\partial p}{\partial y} + (\mu + \mu_t)\left(\frac{\partial^2 v}{\partial x^2} + \frac{\partial^2 v}{\partial y^2} + \frac{\partial^2 v}{\partial z^2}\right) - \rho g_y \tag{16b}$$

$$\rho\left(u\frac{\partial w}{\partial x} + v\frac{\partial w}{\partial y} + w\frac{\partial w}{\partial z}\right) = -\frac{\partial p}{\partial z} + (\mu + \mu_t)\left(\frac{\partial^2 w}{\partial x^2} + \frac{\partial^2 w}{\partial y^2} + \frac{\partial^2 w}{\partial z^2}\right) \tag{16c}$$

where μ and μ_t were the molecular viscosity and turbulent eddy viscosity, respectively.

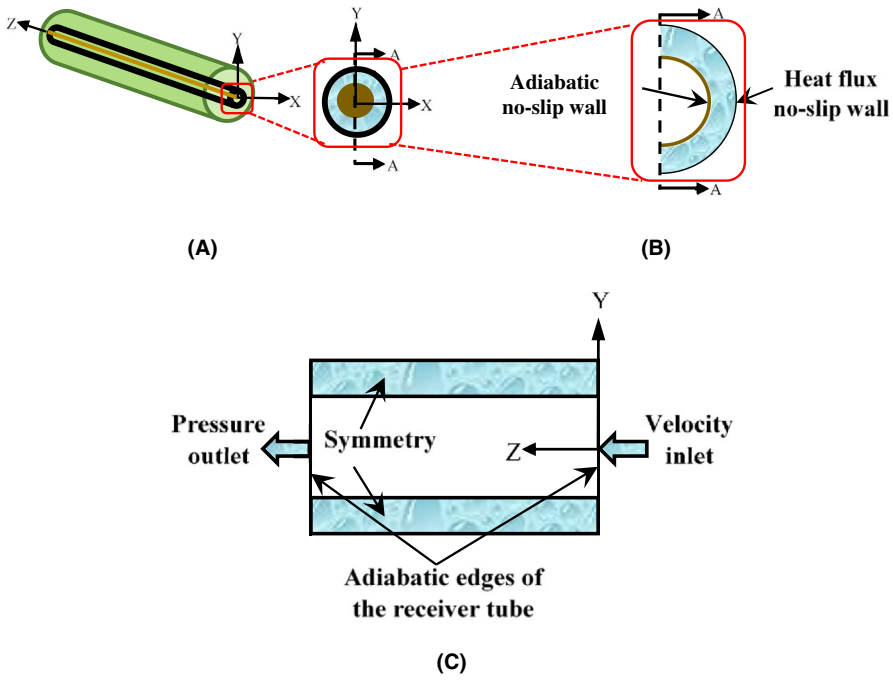

FIGURE 7 Model setup and boundary conditions of HTF domain of the LS2 receiver tube: A, cross section of the receiver tube, B, sectional cross section of the modelled HTF domain, and C, longitudinal view of the modelled HTF domain. (In the figure, A-A is sectional plane)

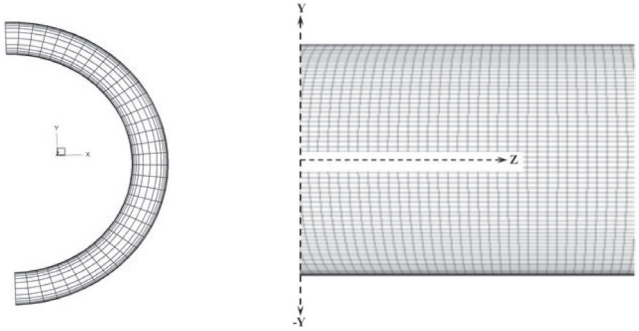

FIGURE 8 Layout of grid distribution of the computational domain: A, at the velocity inlet and pressure outlet and B, at the heat flux wall for the receiver tube and the adiabatic wall for the flow restriction device

The energy balance was given by Equation (17)

$$\rho C_p \frac{\partial T}{\partial t} + \rho C_p \nabla .\left(u_i T\right) = -\nabla_p + \left(k + \frac{C_p \mu_t}{Pr_t}\right) \nabla^2 T + \left(\mu + \mu_t\right) \frac{\partial u_i}{\partial x_j} \left(\frac{\partial u_i}{\partial x_j} + \frac{\partial u_j}{\partial x_i} - \frac{2}{3} \frac{\partial u_k}{\partial x_k} \delta_{ij}\right) + S_r \quad (17)$$

where S_r was the concentrated solar radiation source term.

The turbulent energy production, κ, and the turbulent energy dissipation, ε, for RNG κ-ε model were given by Equation (18) and (19), respectively.

$$\frac{\partial}{\partial t}(\rho\kappa) + \nabla .\left(\rho\kappa u_i\right) = \alpha_\kappa \left(\mu + \mu_t\right) \nabla^2 \kappa + G_\kappa + G_b - \rho\varepsilon \quad (18)$$

$$\frac{\partial}{\partial t}(\rho\varepsilon) + \nabla .\left(\rho\varepsilon u_i\right) = \alpha_\varepsilon \left(\mu + \mu_t\right) \nabla^2 \varepsilon + C_{1s} \frac{\varepsilon}{\kappa} \left(G_\kappa + C_{3\varepsilon} G_b\right) - \rho C_{2\varepsilon}^* \frac{\varepsilon^2}{\kappa} \quad (19)$$

where $C_{1\varepsilon} = 1.42$, $C_{3\varepsilon} = 1.68$, G_κ was turbulent kinetic energy generation for mean velocity gradient, G_b was the same for buoyancy, α_κ is inverse effective Prandtl number for κ, and α_ε was the same for ε.

The modified eddy viscosity for swirl generation for the RNG model was given by Equation (20)

$$\mu_t = \rho C_\mu \frac{\kappa}{\varepsilon} f\left(\alpha_s, \Omega, \frac{\kappa}{\varepsilon}\right) - \rho C_{2\varepsilon}^* \frac{\varepsilon^2}{\kappa} \quad (20)$$

where $C_\mu = 0.0845$ and $\alpha_s \approx 0.07$ were two swirl constants, and Ω was a characteristic swirl number.

4.5 | Heat loss from the ECE wall

The radiation heat loss was calculated by Equation (21)

$$q_{\text{rad}} = \varepsilon\sigma \left[F_{\text{gr}} \left(T_w^4 - T_{\text{gr}}^4\right) + F_{\text{sky}} \left(T_w^4 - T_{\text{sky}}^4\right)\right] \quad (21)$$

where ε was the emissivity of the ECE coating which was given by Equation (22),[31] σ was the Stefan-Boltzmann constant, and F_{gr} and F_{Sky} were the radiation view factors of the ECE with the ground and the sky, respectively, that were calculated as function of ECE angular location, β (see Eq. 23).

$$\varepsilon = 3.27e-4T_w - 6.5971e-2 \quad (22)$$

$$F_{\text{gr}} = 0.5\left(1 + \cos\beta\right) \quad (23a)$$

$$F_{\text{sky}} = 0.5\left(1 - \cos\beta\right) \quad (23b)$$

T_w and T_{Sky} were the average face temperature of each wall cell and sky temperature, respectively. They were calculated by Equation (24).[31]

$$T_{\text{gr}} = T_{\text{amb}} = T_{\text{Sky}} + 8 \quad (24)$$

where T_{amb} is ambient temperature.

Since there was strong wind during the collector testing as Table 4 shows, natural convection heat loss from the ECE was neglected. Heat loss due to forced convection was given by Equation (25).

$$q_{\text{conv}} = h\left(T_{\text{wall}} - T_{\text{amb}}\right) \quad (25)$$

where h was convection coefficient, which was given by the average effect of leeward (h_{lee}) and windward (h_{wind}) convection heat transfer coefficients as the wind flow directions were not known [67] and T_{wall} is the cell average temperature of the heat flux wall surface of the computational domain.

$$h_{\text{lee}} = 2.2V_{\text{amb}} + 8.3 \quad (26a)$$

$$h_{\text{wind}} = 3.3V_{\text{amb}} + 6.5 \quad (26b)$$

4.6 | Algorithm for nonuniform solar energy input and heat loss calculation

The source term, S_r, of Equation (17) was highly nonuniformly distributed concentrated solar irradiation on the wall boundary of the HTF domain (see Figure 7). This was the only constant heat flux source to the domain, and the exact profile of the solar flux, I_β, across the wall surface as shown in Figure 6 was developed in FV model using a source code. At

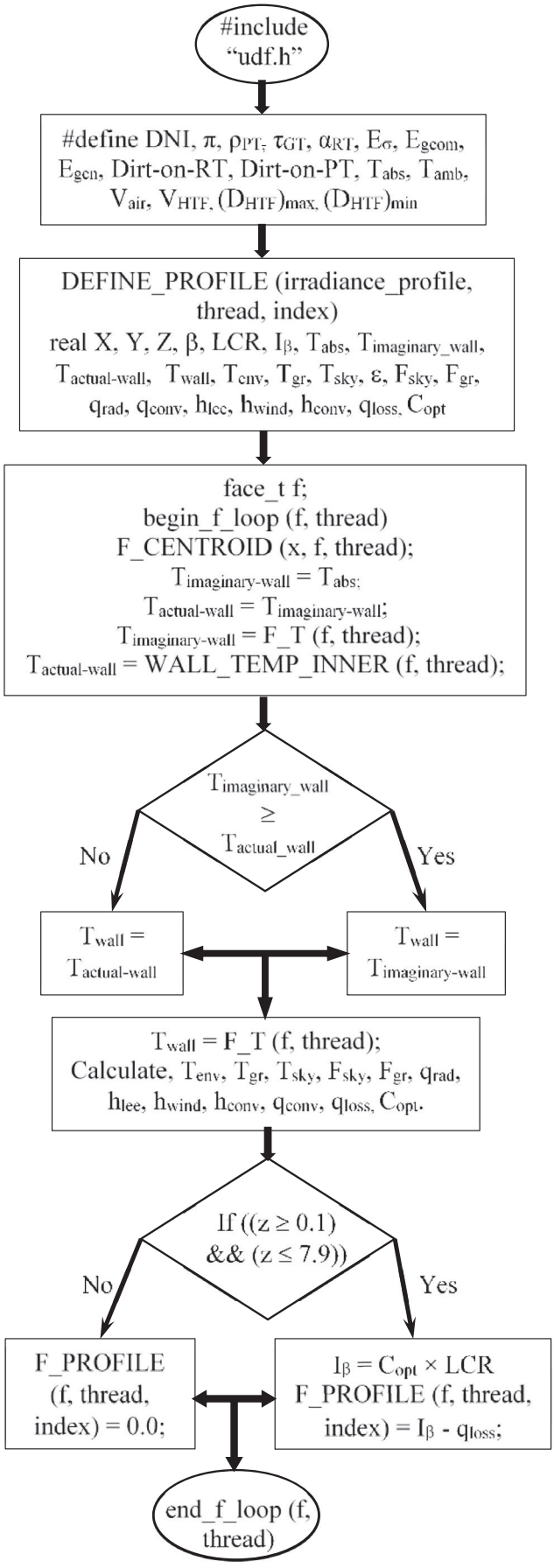

FIGURE 9 Algorithm of the user-defined function. (In the figure, Z is the longitudinal axis of the ECE domain from inlet to outlet. The rest of the notations either are given in the nomenclature, or have their usual meaning in FLUENT subroutine)

ideal condition for the bare ECE, the C_{opt} included the trough reflectance and the ECE absorptance. However, to make the simulation more realistic, factors like tracking error, geometry error, general error, and dust and dirt on the trough and the ECE were also considered in the C_{opt}. Tracking error and geometry error have directional effect on the LCR profile. For simplification, the directional effect on the conjugate heat transfer was neglected, and linear effect on the overall energy efficiency was considered. The values of these loss factors are given in Table 1. Heat loss algorithm was also incorporated in the source code as explained in Figure 9. The rhombuses and the rectangles in the flow chart represent arguments and decisions to the arguments, respectively. The meanings of signs and symbols are either given in the nomenclature or they have usual meaning for the FLUENT subroutine. As the ECE of the LS2 collector was 200 mm larger than the trough, the light was assumed to be concentrated between $Z = 0.1$ m and 7.9 m, and the rest of the ECE was shaded as shown in the last argument of the flowchart.

4.7 | Solution technique

Built-in segregated finite volume method of ANSYS Fluent 14.5 software package was enabled to solve coupled-nonlinear governing equations. As the domain was specified clearly from upstream to downstream, and the cells were hexahedron, convection-diffusion was solved employing a higher order differencing scheme, the QUICK scheme.[68] The "PRESTO!" pressure interpolating scheme and "SIMPLE" pressure-velocity coupling technique were adopted for the current FV model. Under relaxation factor was 0.75 for most of the parameters. However, it was 0.3 for pressure and momentum, and 0.8 for turbulent dissipation rate. Convergence criteria set to maximum 10^{-6} for energy equation and 10^{-4} for the rest of the parameters.

4.8 | Validation of the FV model and verification of the UDF algorithm

4.8.1 | Grid sensitivity test

Static temperature of the receiver wall and plug wall near the HTF outlet for different grid resolutions was recorded from the model as presented in Figure 10. The variation in the temperatures from the grid system $20 \times 80 \times 800$ onward

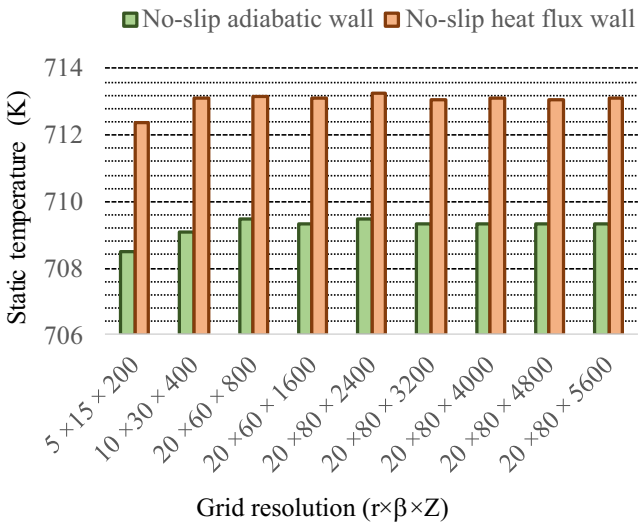

FIGURE 10 Optimum grid resolution

was negligible. Nonetheless, grid structure 20 × 80 × 3200 (=5 120 000 hexahedral cells) was used for this model to obtain a better accuracy in the theoretical results.

4.8.2 | Verification of the, UDF macro, the MCRT coupling algorithm

A test run of the FV model was executed to verify the UDF macro considering 1000 W/m^2 DNI, and the collector was in ideal optical conditions and no heat loss from the outer surface of the computational domain. The residual heat flux profiles across the receiver wall at 0.35 m, 4 m, and 7.23 m length locations from the inlet were calculated and presented in Figure 11. This flux profile is comparable with the input solar flux profile as presented in Figure 6, which confirms the accuracy of the macro, and coupling between the MCRT

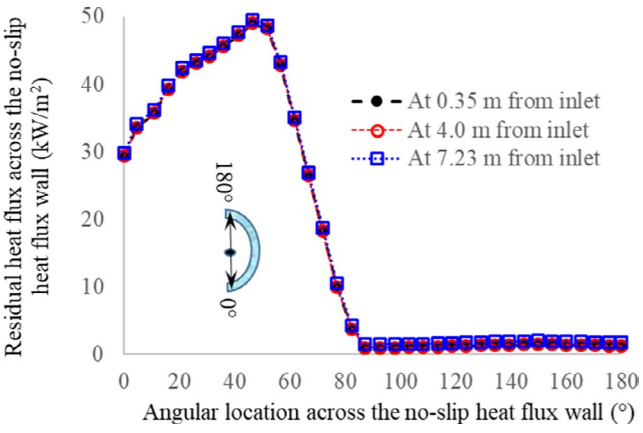

FIGURE 11 Heat flux profiles across the receiver tube at different cross sections from the inlet

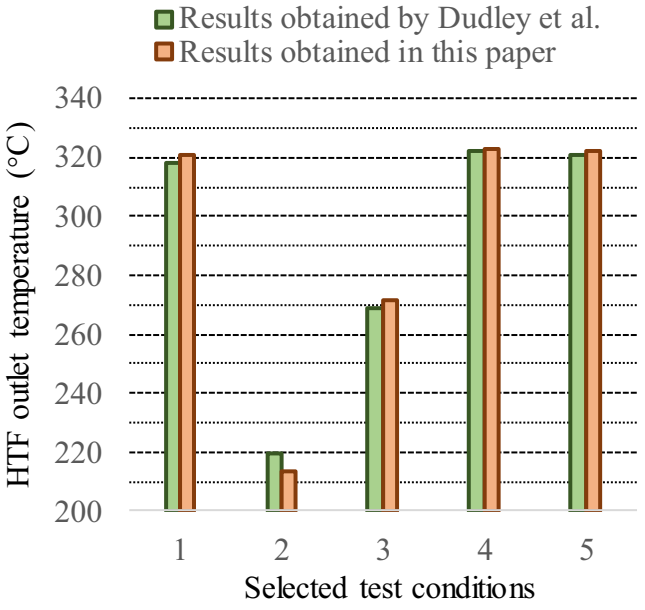

FIGURE 12 Verification of the FV model (Test conditions are in Table 4)

and the current FV model. The flux profiles were found coincident at all three locations because of the fact that the solar flux profile was considered uniform along the length of the ECE.

4.8.3 | Validation of the FV model with experimental results

The HTF outlet temperatures for the selected test conditions (see Table 4) were calculated and compared against the experimental results as shown in Figure 12. The figure shows that the computational results agree very well with their experimental counterparts. The maximum, minimum, and average absolute deviations between the experimental and computational results were found to be 2.92%, 0.23%, and 1.11%, respectively. It could be noted that the maximum deviation was found for the second test condition with lowest DNI (867.6 W/m^2), and so the lowest heat flux density around the no-slip heat flux wall. The DNI for the rest four test conditions was much higher than the second one, DNI varied between 919 and 961 W/m^2, and the ambient air flow was between as low as 0.1 m/s and as high as 9.3 m/s. Average absolute deviation between the experimental and computational results for these four test conditions was only 0.66%. This infers that the heat loss algorithm of this current model is highly capable to predict heat loss at wide range of air speed for high heat flux condition than low heat flux condition. The heat loss algorithm overestimates the heat loss at lower heat flux density. Overall, the current FV model is quite accurate for the simulated PTC.

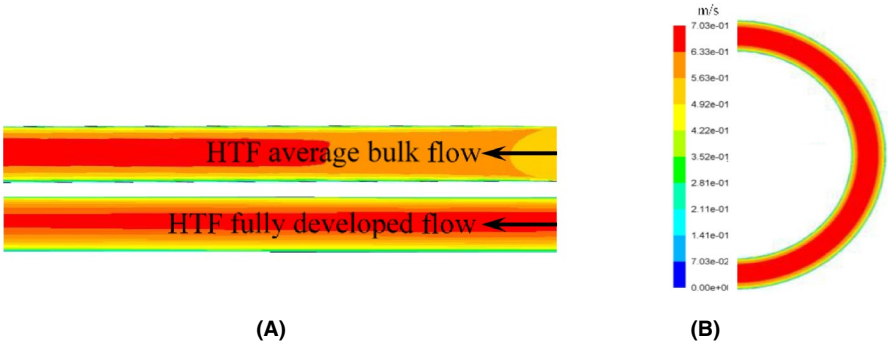

FIGURE 13 Difference between fully developed flow and average bulk flow at the velocity inlet boundary condition: A, velocity profile at the symmetry for both conditions and B, fully developed flow contour at the inlet that considered in the current model

4.8.4 | Verifying fully developed velocity inlet

For this simulation, the HTF domain was considered a part of a continuous fluid line; therefore, the flow must be fully developed throughout the domain. Comparative velocity profile of the HTF at the symmetry of the computational domain for the fully developed flow at the inlet in opposed to an average bulk fluid flow and the resultant velocity profile at the inlet are shown in Figure 13.

5 | TYPICAL APPLICATION OF THE FV MODEL

Using the present FV model, the temperature profile across and heat loss from the receiver tube were calculated as explained below.

5.1 | Temperature profile along the angular direction of the receiver

Static temperature profiles across the receiver wall at 0.35 m, 4 m, and 7.23 m length locations from the inlet were calculated and presented in Figure 14. The temperature profiles were found highly nonuniform and reasonably similar to corresponding input solar flux profile (see Figure 6). The local temperatures were found increasing almost linearly from inlet to the outlet.

5.1.1 | Convection and radiation heat loss from the receiver wall

At outdoor condition, while wind was blowing, the receiver without glass envelop was experiencing forced convection heat loss from its outer surface, as well as radiation heat loss due to high temperature gradient with the ambient. Employing the current FV model, outlet temperatures for the test conditions shown in Table 4 were further modelled assuming: (a) no heat loss, (b) radiation heat loss, (c) convection heat loss, and (d) total (radiation + convection) heat loss. HTF outlet temperatures were recorded as presented in Figure 15.

As Figure 15A shows, HTF outlet temperature for the radiation heat loss model is very close to that of no heat loss model. On the other hand, HTF outlet temperature for the convection heat loss model is very close to that of the total heat loss model. That means convection heat loss from the ECE was accounted for most of the energy loss and was dominated almost linearly by the ambient wind speed (see Figure 15B). Radiation loss on the contrary was very low and dependent on the inlet temperature. Total radiation and convection heat loss were found to be between 18% and 62% of the input energy for the range of ambient wind velocity between 0.1 m/s and 9.3 m/s. The convection heat loss was accounted for 13.5%-57.3% of the total heat loss, which indicates that protection of this convection heat loss from the collector in harsh outdoor condition is extremely important.

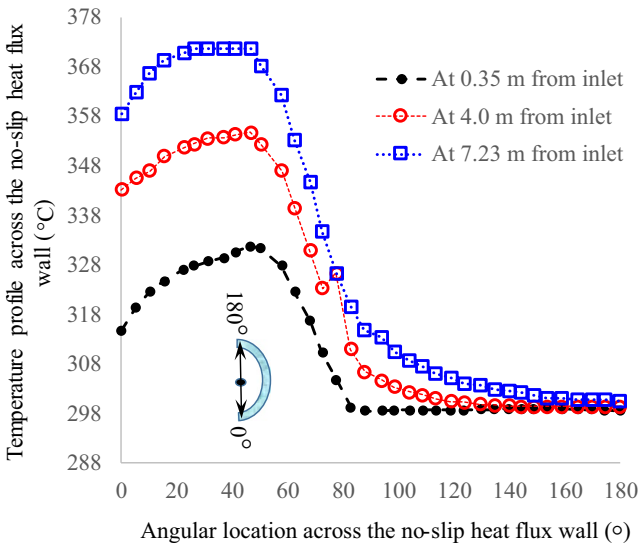

FIGURE 14 Temperature profiles across the receiver tube at different cross sections from the inlet

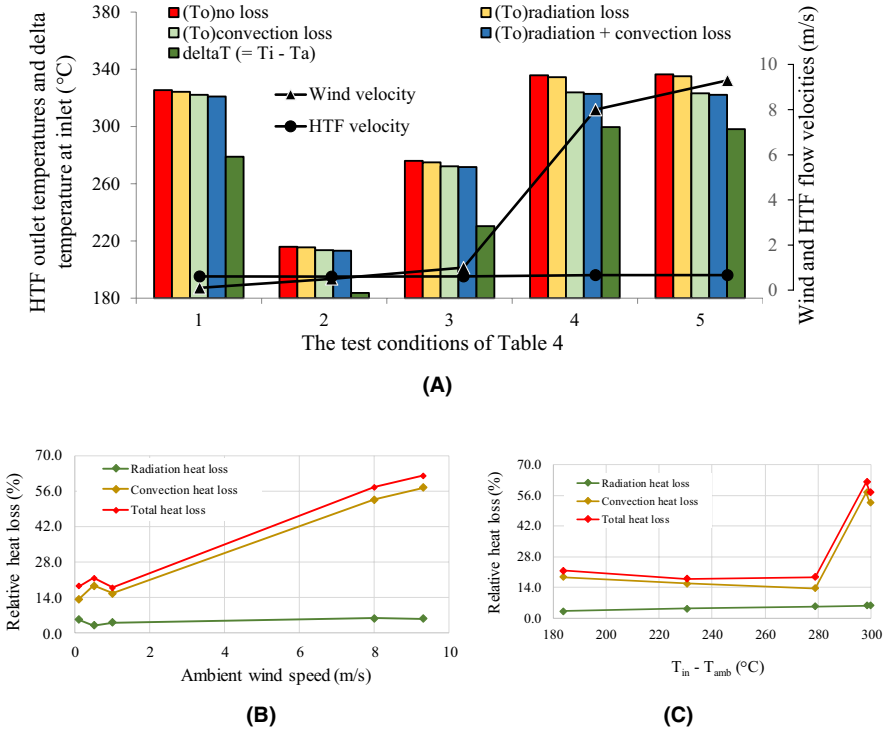

FIGURE 15 A, Estimated outlet temperature for all test conditions, and relative heat loss because of radiation and convection at different B, wind speed and C, inlet temperatures

6 | CONCLUSIONS

Perpendicularly incident sun light on the trough aperture of a parabolic trough collector (PTC) is concentrated highly nonuniformly along the circular direction of the receiver tube of the energy collection element (ECE). Luz Solar II (LS2) is a 8 m long standard PTC, which was used in the Solar Energy Generating System III-VII 150 MW plants, Kramer Junction, California, USA, and tested on the AZTRAK rotating platform at SNL.[47] Analysis of conjugate heat transfer mechanism of the ECE of the LS2 collector using three dimensional (3D) finite volume (FV) technique of computational fluid dynamics (CFD) coupled with Monte Carlo ray-tracing (MCRT) is a popular technique. However, this coupled study is computationally expensive and requires expertise in, and access to, a suitable MCRT code, and thus, prohibitive to many CFD researchers. Open literature lack of any study that attempted to either eliminate or minimize the need of this MCRT code for the conjugate study.

In this paper, the authors attempted to provide a tool in a form of user-defined function (UDF) that will minimize the need of MCRT code and will serve as a built-in function to the FV model. The current study can be summarized as:

1. The UDF contains an algorithm to calculate and populate local irradiance, $I(\beta)$, data as heat flux boundary condition around the receiver tube and heat loss from the receiver of the PTC.
2. $I(\beta)$ is calculated multiplying local concentration ratio (LCR) by daily normal irradiance (DNI) and optical factors. The heat loss algorithm accounts for the radiation loss and the convection loss depending on the glass envelop condition.
3. The LCR is a function of angular location, β, of the receiver, derived as polynomial correlations from a validated 3D MCRT model. The optical factors include the optical properties of the collector components and the optical error factors such as tracking error, general error, geometry error, and effect of dirt on the optical surfaces of the collector.
4. The MCRT coupling algorithm of the UDF is verified, and the FV model is validated with experimental results.
5. Typical application of the model was performed by checking temperature profile around the ECE, and radiation and convection heat losses from the ECE. Convection heat loss from the outer surface of the receiver tube (assumed bare or no glass envelop) was dominant over the radiation heat loss and varies almost linearly with ambient wind velocity. For wind velocity ranges between 0.1 and 9.3 m/s, and convection heat loss was observed to be accounted for 13.5%-57.3% out of 18%-62% of total heat loss.
6. The UDF has the capacity to accommodate and use for various
   a. optical conditions include daily normal irradiance, optical properties of the collector components, and optical loss factors with average effect, such as, tracking error, effect of dirt and dust on the participating surfaces, general error, and geometry error;
   b. collector geometry that include collector length and internal diameter of the receiver;

c. glass envelop conditions including evacuated, filled of air or removed;
d. internal design of the receiver tube, such as, inserts or swirl generator; and
e. HTFs (such as, oils and nanofluid including molten salt nanofluid), ambient wind speed and temperatures.

ORCID

Majedul Islam https://orcid.org/0000-0002-7601-6901

REFERENCES

1. Kalogirou SA. Solar energy engineering: processes and systems. In: Kalogirou SA, ed. *Solar Energy Engineering*. Boston, MA: Academic Press; 2009:1-48.
2. Yılmaz İH. Optimization of an integral flat plate collector-storage system for domestic solar water heating in Adana. *Anad Univ J Sci Technol A - Appl Sci Eng*. 2018;19:165-176.
3. Yılmaz İH, Mwesigye A. Modeling, simulation and performance analysis of parabolic trough solar collectors: a comprehensive review. *Appl Energy*. 2018;225:135-174.
4. Price H, Lüpfert E, Kearney D, et al. Advances in parabolic trough solar power technology. *J Sol Energy Eng*. 2002;124:109-125.
5. Fernández-García A, Zarza E, Valenzuela L, Pérez M. Parabolic-trough solar collectors and their applications. *Renew Sustain Energy Rev*. 2010;14(7):1695-1721.
6. Mousazadeh H, Keyhani A, Javadi A, Mobli H, Abrinia K, Sharifi A. A review of principle and sun-tracking methods for maximizing solar systems output. *Renew Sustain Energy Rev*. 2009;13(8):1800-1818.
7. Parida B, Iniyan S, Goic R. A review of solar photovoltaic technologies. *Renew Sustain Energy Rev*. 2011;15(3):1625-1636.
8. Timilsina GR, Kurdgelashvili L, Narbel PA. Solar energy: markets, economics and policies. *Renew Sustain Energy Rev*. 2012;16(1):449-465.
9. Tyagi VV, Kaushik SC, Tyagi SK. Advancement in solar photovoltaic/thermal (PV/T) hybrid collector technology. *Renew Sustain Energy Rev*. 2012;16(3):1383-1398.
10. Pavlović TM, Radonjić IS, Milosavljević DD, Pantić LS. A review of concentrating solar power plants in the world and their potential use in Serbia. *Renew Sustain Energy Rev*. 2012;16(6):3891-3902.
11. Devabhaktuni V, Alam M, Shekara Sreenadh Reddy Depuru S, Green RC, Nims D, Near C. Solar energy: trends and enabling technologies. *Renew Sustain Energy Rev*. 2013;19:555-564.
12. Cabrera FJ, Fernández-García A, Silva R, Pérez-García M. Use of parabolic trough solar collectors for solar refrigeration and air-conditioning applications. *Renew Sustain Energy Rev*. 2013;20:103-118.
13. Zhang HL, Baeyens J, Degrève J, Cacères G. Concentrated solar power plants: review and design methodology. *Renew Sustain Energy Rev*. 2013;22:466-481.
14. Mojiri A, Taylor R, Thomsen E, Rosengarten G. Spectral beam splitting for efficient conversion of solar energy—a review. *Renew Sustain Energy Rev*. 2013;28:654-663.
15. Jebasingh VK, Herbert GMJ. A review of solar parabolic trough collector. *Renew Sustain Energy Rev*. 2016;54:1085-1091.
16. Islam M, Karim A, Saha SC, Yarlagadda PK, Miller S, Ullah I. Visualization of thermal characteristics around the absorber tube of a standard parabolic trough thermal collector by 3D simulation. In *Proceedings of the 4th International Conference on Computational Methods (ICCM2012)*. Crowne Plaza, Gold Coast, Australia: School of Chemistry, Physics and Mechanical Engineering, Queensland University of Technology; 2012.
17. Islam M, Karim M, Saha SC, Miller S, Yarlagadda PKDV. Development of empirical equations for irradiance profile of a standard parabolic trough collector using Monte Carlo ray tracing technique. *Adv Mater Res*. 2014;860–863:180-190.
18. Islam M, Sadi M, Limon AH, Faruque MO, Yarlagadda PKDV. Manufacturing of a parabolic trough concentrating collector test rig and a "LASER-Screen" technique for measuring actual focal length and light interceptance of the collector. *Proc Manuf*. 2019;30:404-410.
19. Karim M, Arthur O, Yarlagadda P, Islam M, Mahiuddin Md. Performance investigation of high temperature application of molten solar salt nanofluid in a direct absorption solar collector. *Molecules*. 2019;24(2):285.
20. Karim M, Islam M, Arthur O, Yarlagadda PK. Performance of graphite dispersed Li2CO3-K2CO3 molten salt nanofluid for direct absorption solar collector. *Molecules*. 25(2):375.
21. Islam M, Yarlagadda P, Karim A. Effect of the orientation schemes of the energy collection element on the optical performance of a parabolic trough concentrating collector. *Energies*. 2018;12(1):128.
22. Islam M, Islam MdI, Tusar M, Limon AH. Effect of cover design on moisture removal rate of a cabinet type solar dryer for food drying application. *Energy Procedia*. 2019;160:769-776.
23. IEA. Renewable Energy Essentials: Concentrating Solar Thermal Power. 2009.
24. Duffie JA, Beckman WA. *Solar Engineering of Thermal Processes*. 4th ed. Solar Engineering. New York, USA: Wiley; 2013.
25. Behar O, Khellaf A, Mohammedi K. A novel parabolic trough solar collector model – Validation with experimental data and comparison to Engineering Equation Solver (EES). *Energy Convers Manage*. 2015;106:268-281.
26. Kalogirou SA. Solar thermal collectors and applications. *Prog Energy Combust Sci*. 2004;30(3):231-295.
27. Kalogirou SA. A detailed thermal model of a parabolic trough collector receiver. *Energy*. 2012;48(1):298-306.
28. Tzivanidis C, Bellos E, Korres D, Antonopoulos KA, Mitsopoulos G. Thermal and optical efficiency investigation of a parabolic trough collector. *Case Studies in Thermal Engineering*. 2015;6:226-237.
29. Islam M, Miller S, Yarlagadda P, Karim A. Investigation of the effect of physical and optical factors on the optical performance of a parabolic trough collector. *Energies*. 2017;10(11):1907.
30. Jeter SM. Calculation of the concentrated flux density distribution in parabolic trough collectors by a semifinite formulation. *Sol Energy*. 1986;37(5):335-345.
31. Forristall R. *Heat Transfer Analysis and Modeling of a Parabolic Trough Solar Receiver Implemented in Engineering Equation Solver*. 1617 Cole Boulevard Golden, Colorado 80401-3393: National Renewable Energy Laboratory; 2003. Technical report No. NERL/TP-550-34169.
32. Riffelmann K-J, Neumann A, Ulmer S. Performance enhancement of parabolic trough collectors by solar flux measurement in the focal region. *Sol Energy*. 2006;80(10):1303-1313.
33. Schiricke B, Pitz-Paal R, Lüpfert E, et al. Experimental verification of optical modeling of parabolic trough collectors by flux measurement. *J Sol Energy Eng*. 2009;131(1): 011004
34. Jeter SM. The distribution of concentrated solar radiation in paraboloidal collectors. *J Sol Energy Eng*. 1986;108(3):219-225.

35. Jeter SM. Analytical determination of the optical performance of practical parabolic trough collectors from design data. *Sol Energy*. 1987;39(1):11-21.
36. Cheng ZD, He YL, Cui FQ. A new modelling method and unified code with MCRT for concentrating solar collectors and its applications. *Appl Energy*. 2013;101:686-698.
37. Cheng ZD, He YL, Cui FQ, Xu RJ, Tao YB. Numerical simulation of a parabolic trough solar collector with nonuniform solar flux conditions by coupling FVM and MCRT method. *Sol Energy*. 2012;86(6):1770-1784.
38. He Y-L, Xiao J, Cheng Z-D, Tao Y-B. A MCRT and FVM coupled simulation method for energy conversion process in parabolic trough solar collector. *Renewable Energy*. 2011;36(3):976-985.
39. Grena R. Optical simulation of a parabolic solar trough collector. *Int J Sustain Energ*. 2009;29(1):19-36.
40. Daly JC. Solar concentrator flux distributions using backward ray tracing. *Appl. Opt*. 1979;18(15):2696-2699.
41. Yang B, Zhao J, Xu T, Zhu Q, et al. Calculation of the concentrated flux density distribution in parabolic trough solar concentrators by Monte Carlo Ray-Trace Method. In *Photonics and Optoelectronic (SOPO) Symposium*. Chengdu, China : IEEE; 2010;1–4. https://ieeexplore.ieee.org/document/5504452
42. Zou B, Dong J, Yao Y, Jiang Y. A detailed study on the optical performance of parabolic trough solar collectors with Monte Carlo Ray Tracing method based on theoretical analysis. *Sol Energy*. 2017;147:189-201.
43. Cheng ZD, He YL, Cui FQ, Du BC, Zheng ZJ, Xu Y. Comparative and sensitive analysis for parabolic trough solar collectors with a detailed Monte Carlo ray-tracing optical model. *Appl Energy*. 2014;115:559-572.
44. Kalogirou S. The potential of solar industrial process heat applications. *Appl Energy*. 2003;76(4):337-361.
45. Kalogirou SA, Lloyd S, Ward J, Eleftheriou P. Design and performance characteristics of a parabolic-trough solar-collector system. *Appl Energy*. 1994;47(4):341-354.
46. Soteris K. The potential of solar industrial process heat applications. *Appl Energy*. 2003;76(4):337-361.
47. Dudley VE, Kolb GJ, Mahoney AR et al. Test Results: SEGS LS-2 Solar Collector, pp. 139; 1994.
48. Islam M, Karim A, Saha SC, Miller S, Yarlagadda PKDV. Three dimensional simulation of a parabolic trough concentrator thermal collector. in *Blume, S (Ed.) Proceedings of the 50th Annual Solar Conference, Australian Solar Energy Society (AuSES)*, 6-7 December. Australia: Australian Solar Council; 2012.1–11.
49. Karim MA, Hawlader MNA. Performance evaluation of a v-groove solar air collector for drying applications. *Appl Therm Eng*. 2006;26(1):121-130.
50. Karim MA, Hawlader MNA. Performance investigation of flat plate, v-corrugated and finned air collectors. *Energy*. 2006;31(4):452-470.
51. Karim MA, Hawlader MNA. Development of solar air collectors for drying applications. *Energy Convers Manage*. 2004;45(3):329-344.
52. Islam M, Saha SC, Karim A, Yarlagadda PKDV. A Method of Three-Dimensional Thermo-Fluid Simulation of the Receiver of a Standard Parabolic Trough Collector. In: Khan MMK, Chowdhury AA, Hassan NMS, eds. *Application of Thermo-fluid Processes in Energy Systems: Key Issues and Recent Developments for a Sustainable Future*. Singapore: Springer Singapore; 2018:203-230. https://link.springer.com/chapter/10.1007/978-981-10-0697-5_9.
53. Cheng ZD, He YL, Xiao J, Tao YB, Xu RJ. Three-dimensional numerical study of heat transfer characteristics in the receiver tube of parabolic trough solar collector. *Int Commun Heat Mass Transfer*. 2010;37(7):782-787.
54. García-Valladares O, Velázquez N. Numerical simulation of parabolic trough solar collector: Improvement using counter flow concentric circular heat exchangers. *Inte J Heat Mass Transfer*. 2009;52(3):597-609.
55. Padilla RV, Demirkaya G, Goswami DY, Stefanakos E, Rahman MM. Heat transfer analysis of parabolic trough solar receiver. *Appl Energy*. 2011;88(12):5097-5110.
56. Yılmaz İH, Söylemez MS. Thermo-mathematical modeling of parabolic trough collector. *Energy Convers Manage*. 2014;88:768-784.
57. Liang H, You S, Zhang H. Comparison of different heat transfer models for parabolic trough solar collectors. *Appl Energy*. 2015;148:105-114.
58. Tao YB, He YL. Numerical study on coupled fluid flow and heat transfer process in parabolic trough solar collector tube. *Sol Energy*. 2010;84(10):1863-1872.
59. Hachicha AA, Rodríguez I, Capdevila R, Oliva A. Heat transfer analysis and numerical simulation of a parabolic trough solar collector. *Appl Energy*. 2013;111:581-592.
60. Wang P, Liu DY, Xu C, Zhou L, Xia L. Conjugate heat transfer modeling and asymmetric characteristic analysis of the heat collecting element for a parabolic trough collector. *Int J Therm Sci*. 2016;101:68-84.
61. Huang W, Xu Q, Hu P. Coupling 2D thermal and 3D optical model for performance prediction of a parabolic trough solar collector. *Sol Energy*. 2016;139:365-380.
62. Wirz M, Roesle M, Steinfeld A. Three-dimensional optical and thermal numerical model of solar tubular receivers in parabolic trough concentrators. *J Sol Energy Eng*. 2012;134(4):363-373.
63. *ANSYS FLUENT Theory Guide. Release 15.0*. Southpointe, 275 Technology Drive, Canonsburg, PA 15317 USA: ANSYS, Inc.; 2013. https://www.scribd.com/document/446961562/ANSYS-Fluent-Theory-Guide-15-pdf.
64. Beard J, Iachetta F, Lilleleht L, Huckstep F, May W. Design and operational influences on thermal performance of "Solaris" solar collector. *Journal of Engineering for Power*. 1978;100(4):497-502.
65. . *Syltherm 800, Heat Transfer Fluid: Product Technical Data*. USA: DOW Chemcal Company; 1997:1–28. https://www.dow.com/content/dam/dcc/documents/en-us/app-tech-guide/176/176-01435-01-syltherm-800-heat-transfer-fluid.pdf?iframe=true.
66. Launder BE, Spalding DB. The numerical computation of turbulent flows. *Comput Methods Appl Mech Eng*. 1974;3(2):269-289.
67. Sharples S, Charlesworth PS. Full-scale measurements of wind-induced convective heat transfer from a roof-mounted flat plate solar collector. *Sol Energy*. 1998;62(2):69-77.
68. Leonard BP, Mokhtari S. Beyond first-order upwinding: The ultra-sharp alternative for non-oscillatory steady-state simulation of convection. *Int J Numer Meth Eng*. 1990;30(4):729-766.

How to cite this article: Islam M, Saha SC, Yarlagadda PKDV, Karim A. A tool to minimize the need of Monte Carlo ray tracing code for 3D finite volume modelling of a standard parabolic trough collector receiver under a realistic solar flux profile. *Energy Sci Eng*. 2020;8:3087–3102. https://doi.org/10.1002/ese3.741